**THE EUROPEAN
PHYSICAL JOURNAL PLUS**

Regular Article

Ag@AgCl/Cu²⁺-Bi₂O₃ nanocomposite for decontamination of Rhodamine B: adsorption, kinetics, thermodynamics, and photocatalytic aspects

Anuradha Sharma[1]**, Shankar Sharma**[1]**, Peter R. Makgwane**[2,3,a]**, Vijaya Kumari**[1]**, Kavitha Kumari**[4]**, Jyoti Kataria**[5]**,
Naveen Kumar**[1,b]

[1] Department of Chemistry, Maharshi Dayanand University, Rohtak 124001, India
[2] Centre for Nanostructures and Advanced Materials, Council for Scientific and Industrial Research (CSIR), Pretoria 0001, South Africa
[3] Department of Chemistry, University of the Western Cape, Robert Sobukwe Drive, Bag X17, Bellville 7535, South Africa
[4] Department of Chemistry, Baba Mastnath University, Rohtak 124001, India
[5] Department of Chemistry, Guru Jambheshwar University of Science & Technology, Hisar 125001, India

Abstract A novel Ag@AgCl decorated Cu²⁺- Bi₂O₃ nanocomposite was successfully constructed by fastening Ag and AgCl nanocrystals onto the surface of Cu²⁺- Bi₂O₃ nanoparticles via the simple precipitation-deposition process. The synthesized products were characterized thoroughly by using different techniques; in terms of their structural features (XRD), morphological characteristics (SEM), constitutional elements (EDX and XPS), optical (UVDRS and PL), chemical bonding (FTIR), and photocatalytic properties. Highly crystalline and pure compounds were indicated by the XRD analysis. The SEM, EDX, and XPS analysis confirmed the flake-like morphology, high purity, and constitutional elements with their chemical states in the as-synthesized sample. The optical band gap energies (3.33–3.59 ev) were estimated with UV–Vis DRS analysis and PL spectra were recorded to analyze the fluorescence emission. The adsorption and catalytic performance of the prepared catalysts were tested for model organic pollutant RhB dye. Adsorption aspects were studied in terms of adsorption kinetic, isotherm, and thermodynamic models. Adsorption phenomenon was best explained by using the Langmuir isotherm ($R^2 = 0.997$) and pseudo second-order kinetics models ($R^2 = 0.984$). Moreover, in the thermodynamic parameters, negative values of $\Delta H°$ (-61.13 kJ/mol) and $\Delta G°$ (-0.619 kJ/mol) indicated exothermic and spontaneous adsorption, respectively at the lower temperatures. As photocatalyst, Ag@AgCl/Cu²⁺-Bi₂O₃ nanocomposites exhibited superior performance (99.60% degradation in $60 min$) compared to the binary Cu²⁺-Bi₂O₃ sample (81.48%) for RhB removal. The role of pH and active species involved in the degradation process were also analyzed.

1 Introduction

Environmental issues assisted with the toxic organic contaminants in aqua-bodies drive the researchers for continuous investigations in the sector of environmental science [1, 2]. In this direction, adsorption and thereupon photocatalysis is an efficient and feasible method that employs semiconductor materials to decompose several types of pollutants under light radiations [3–7]. Among different semiconductor catalysts, bismuth oxide (Bi₂O₃) is an adequate candidate in photocatalysis owing to its chemical stability, non-toxicity, and high abundance in our country. Also, this material's optical band energy gap can be tuned from 1.7 to 3.9 eV according to the synthesis conditions and crystalline phases produced in the material. In addition, the orbital hybridization between $6s$ orbitals of Bi and $2p$ orbitals of the O atoms in Bi₂O₃, respectively supports the photoinduced holes to move onto the *valence band* of Bi₂O₃ which interrupts the reunion of photo-generated charged species [8, 9]. To further enhance the catalytic efficiency of Bi₂O₃, a number of methods including noble metals deposition [10], doping of metal ions [11], reshaping morphology [12], and making composites [13, 14] have been reported in literature out of which doping and composite formation are the effective ways for better separation of light-induced electron and hole pairs [6, 15]. Further, literature reported Ag/AgX (where X may be Cl, Br, and I) structures as stable and efficient photocatalysts that also exhibit the property of behaving as co-catalysts. A few of co-relative catalysts have also been reported including Ag/AgCl/TiO₂ [16], Ag/AgBr/WO₃ [17], Ag/AgCl-CeO₂ [18], Ag − AgCl@Bi₂₀TiO₃₂ [19], and Ag/AgCl-Bi₂WO₆ [20] and are found efficient in the removal of different organic contaminants. The obtained results indicated that the Ag@AgX works efficiently both as a catalyst and co-catalyst.

Inspired by these above mentioned works, we synthesized a novel Ag@AgCl decorated Cu²⁺- Bi₂O₃ nanocomposite and RhB solution was taken as the model pollutant to study adsorption and photo-activity of the prepared compounds. Different parameters influencing adsorption along with the adsorption isotherm models, kinetic models, and the involved thermodynamic parameters were

[a] e-mails: pmakgwane@csir.co.za; makgwane.peter@gmail.com

[b] e-mail: naveenkumar.chem@mdurohtak.ac.in (corresponding author)

Springer

also investigated. The results indicated that addition of even a small amount of Ag/AgCl could significantly enhanced the catalytic efficiency of binary Cu^{2+}- Bi_2O_3 composite. The relationship of photodegradation efficiency with the structural properties of the synthesized materials was examined via a systematized characterization study, and also a probable mechanism of the degradation reaction is presented.

2 Experimental

2.1 Materials

Nitrates of bismuth and copper [$Bi(NO_3)_3.5H_2O$, 99.9%] and [$Cu(NO_3)_2.3H_2O$, 99.9%], NaOH and HNO_3 were obtained from CDH chemicals. Silver nitrate [$AgNO_3$, 99.9%] a source of silver and a model pollutant [RhBdye, 95%] were used from Sigma Aldrich, India. [KCl, 99% and [$NaBH_4$, 96%] were taken for the precipitation and reduction purposes respectively. Double distilled water was used in the laboratory for whole experimentation.

2.2 Preparation of photocatalyst

2.2.1 Synthesis of binary Cu doped Bi₂O₃ (BC-2) nanocomposite

The BC-2 photocatalyst (2 mol % Cu in Bi_2O_3 lattice) was synthesized by using hydrothermal method [15]. Initially, 4.7536 g of bismuth nitrate was stirred in 1 M aqueous HNO_3 solution (40ml) at a constant temperature for 30min. Then NaOH solution was added drop by drop for precipitation and stirred for $60min$. Then, calculated amount of copper nitrate (0.04832 g) was put in, to obtain the desired ratio and stirred further for 60min. The resulting solution was then transferred for hydrothermal procedure for 16 h at 180 °C. The prepared sample was then filtered, dried and collected.

2.2.2 Synthesis of ternary Ag/AgCl decorated BCA nanocomposites

To synthesize ternary composites, further modifications were done on the pre-prepared binary BC-2 sample by following a simple chemical route. 1 g of BC-2 was stirred for 30 min on a magnetic stirrer taken in 50 ml water at a speed of 1000 rpm. After obtaining a homogeneous medium, $AgNO_3$ (0.1 mmol) was added and stirred for further 30 min. After that calculated amount of KCl(0.05 mmol) was added followed by 30 min stirring. Formation of white coloured precipitates confirmed the formation of AgCl. The remaining Ag^+ ions (0.05 mmol) were reduced with the help of $NaBH_4$ solution. The colour of solution turned greyish black that assured the formation of silver nanoparticles, deposition of which on BC-2 lead to formation of ternary photocatalyst. The product was then filtered, washed and dried. This equimolar $Ag - AgCl$ (0.05–0.05 mmol) compound was named as BCA-2. The corresponding 0.1 mmol AgCl and 0.1 mmolAg were also synthesized by following the similar procedure for comparison study and labelled as BCA-1 and BCA-3 respectively. All the samples are presented with description in the Table 1.

2.3 Characterizations

The prepared nanocomposite samples were characterized and analyzed by the help of different characterization techniques. XRD patterns of the synthesized samples was used to estimate the phase structures and crystallinity of the compounds. The patterns were recorded in the 2θ (20–80°). SEM technique was used to determine the morphological and surface characteristics of the compounds. The EDX- spectroscopy was employed for the determination of elemental composition. UV–vis DRS recorded on Shimadzu 3600 plus spectrophotometer was used to determine the optical properties of the synthesized materials. Both absorbance and reflectance were obtained from the same instrument. Band gap analysis was done with the help of Kubelka–Munk equation where plots were drawn by following the same equation. XPS was used to identify the elemental as well as ionic constitution in the compounds on (Physical Electronics, PHI 5000 Versa Probe III) instrument. Photoluminescence spectra of synthesized compounds were taken to justify the separation of generated charge carriers by using fluorescence spectrophotometer (Hitachi F-7000). The bonding conditions

Table 1 All the synthesized composites with constituents and compositions

Sample name	Constituents	Composition
BC-2	Cu^{2+}, Bi_2O_3	2 mol% Cu^{2+} in Bi_2O_3
BCA-1	Cu^{2+}, Bi_2O_3, AgCl	0.1 mmol AgCl
BCA-2	Cu^{2+}, Bi_2O_3, Ag, AgCl	(0.05–0.05) mmol Ag–AgCl
BCA-3	Cu^{2+}, Bi_2O_3, Ag	0.1 mmol Ag

in the samples were analyzed with the help of Fourier transform infrared spectrometer (Nicolet iS50 FTIR). Surface charge of the materials was also obtained on a (Zetasizer Ver. 7.13) zeta potential (ζ) analyzer.

2.4 Photocatalytic activity

Photocatalytic efficiency of the synthesized materials was determined by the degradation of RhB. The photocatalytic experiments were conducted in a photochemical reactor under the exposure of xenon lamp (125 W) at 25 °C. 50 mg catalyst was added in 100 ml of the dye (10 ppm) solution and stirred for one hour in dark for equilibrium. After this, the process was then followed by UV light illumination and oxygen was supplied with the help of an air bubbler. Nearly 5 ml solution from the reaction mixture was withdrawn at definite intervals of time and centrifuged. The supernatant was analyzed on a UV–vis absorption spectrophotometer to estimate the concentrations of dye solutions by taking the absorbance at $\lambda_{max} = 553$nm. The photo removal efficiency of the photocatalyst was then computed with the help of the calculated dye concentration values. The active species generated during the degradation process were also assessed by the adding the different scavengers like BQ (benzoquinone), IPA (isopropyl alcohol), and EDTA (ethylenediammine tetra acetic acid) with the catalyst.

2.5 Statistical section

The presented values of adsorption and photodegradation experiments in the present work were taken in average of three repeated experiments. Adsorption isotherm and kinetic parameters, standard deviations and errors, and correlation coefficient (R^2) were all measured with the Microsoft Excel 2013. All the figures were designed with the help of Origin 9.0 program and error bars were presented within all the figures.

3 Result and discussion

3.1 XRD

To explore the structure and phases of synthesized materials, XRD patterns were recorded and are demonstrated in the Fig. 1. The diffraction peaks obtained at 2θ of 25.46, 33.09, 39.54, 48.73° are in agreement with the diffraction planes (002), (121), (222), and (104) of the monoclinic α-Bi_2O_3 phase (PDF NO.6–294) [21]. The other peaks observed at 2θ = 28.08, 31.31, 46.21, 54.75, 65.33, and 58.13° are ascribed to the (201), (002), (222), (203), (400), and (402) planes of tetragonal β-Bi_2O_3 (PDF NO. 27–50) [22, 23]. Further, doping of Cu^{2+} ions was confirmed by the fact that all the samples exhibited the specific peaks of Bi_2O_3 and no peak corresponds to CuO was seen in the spectra. In addition, no shifting in the peaks was observed that again supports the lattice doping of Cu^{2+} ions since ionic radii of Cu^{2+} ions being 0.073 nm is smaller than that of the Bi^{3+} ions which is equal to 0.103 nm [24]. Quantitative analysis was done with the help of Rietveld treatment method where close to 33 and 67% α- monoclinic and β-tetragonal Bi_2O_3 phases were obtained. Further, Ag and AgCl could not be identified in the recorded patterns. This is because of very low content and peaks were too weak to be identified. Next, Scherrer's equation [25] was employed to calculate the crystallite sizes that were found 31, 36, 42, 38 nm for BC-2, BCA-1, BCA-2, and BCA-3 respectively.

Fig. 1 X- Ray Diffraction patterns of BC-2 and different BCA nanocomposites
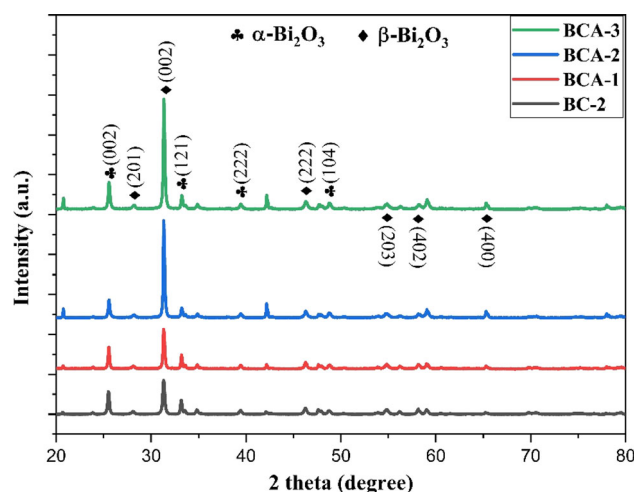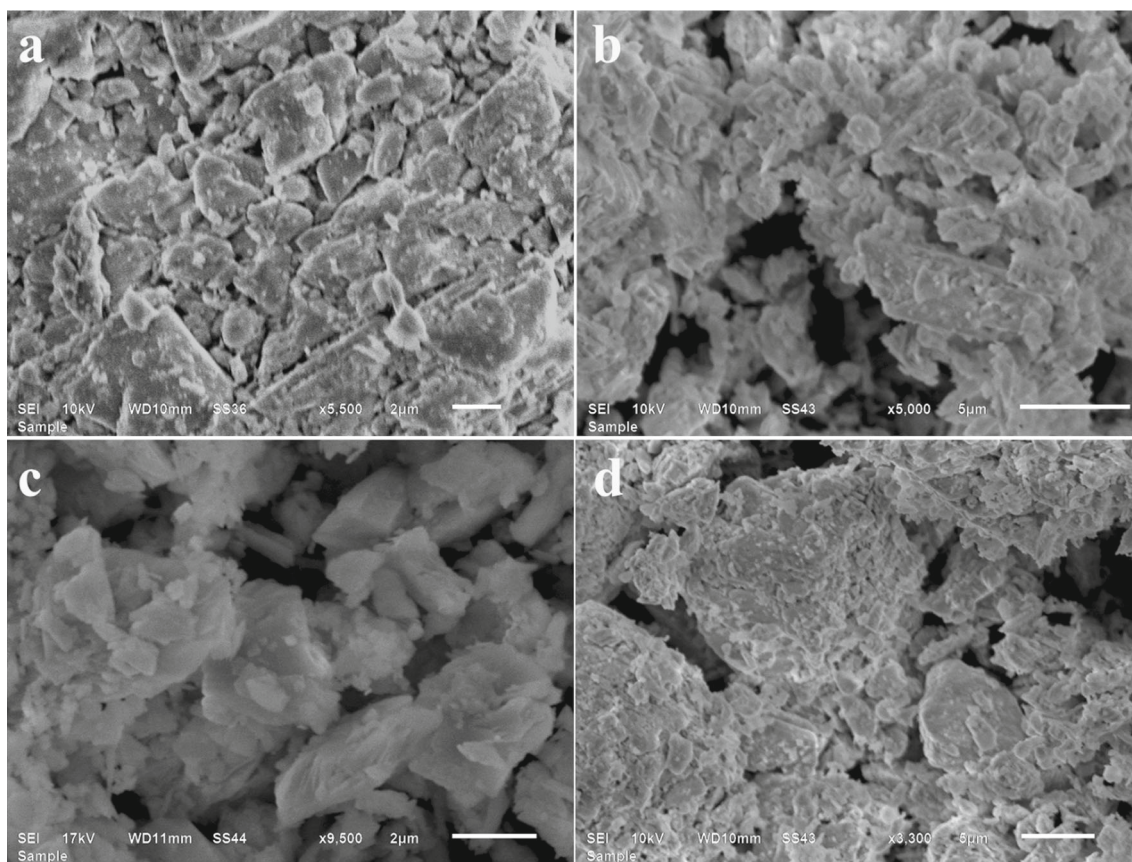
Fig. 2 SEM micro- images of **a** binary BC-2, **b** BCA-1, **c** BCA-2, and **d** BCA-3 nanocomposites

3.2 Morphological and elemental analysis (SEM and EDX)

The SEM pictures of binary BC-2 and all the ternary BCA- samples are shown in the Fig. 2. The BC-2 sample consist of aggregated irregular clusters whereas flake like characteristics are observed in the ternary BCA-2 sample [26]. Next, elemental constitution was identified with EDX analysis and depicted in Fig. 3. No additional peaks were seen in the spectra which confirms the purity of prepared materials. Moreover, Fig. 3 displays the mapping images of the present elements which is clearly showed that the constituent particles present in the product are uniformly dispersed.

3.3 XPS

The chemical composition and elemental states of the BCA-2 nanocomposite were analysed by using XPS, as presented in the Fig. 4. Survey spectrum in Fig. 4a confirmed the existence of Bi, Cu, O, Ag, and Cl elements. Carbon 1s spectra was used for calibration at binding energy 284.64 eV (Fig. 4b). The high resolution spectra of Bi element (Fig. 4c) shows two signals at 164.23 and 158.89 eV which correspond to Bi $4f_{5/2}$ and Bi $4f_{7/2}$ levels respectively [27]. The two peaks in the oxygen 1s spectrum obtained at 529.62 and 531.41 eV (Fig. 4d) indicate the presence of two different chemical states of oxygen atoms. The first one at 529.62 eV corresponds to lattice O in the material in -2 state while the second one obtained at 531.41 eV can be deemed as the atoms present in the vicinity of oxygen vacancies [28]. The peak obtained at binding energy of 942.36 eV corresponds to the Cu $2p_{3/2}$ level that indicates the presence of + 2 oxidation state of copper ions (Fig. 4e). This peak is assigned as the satellite signal for $2p_{3/2}$ level [29]. This kind of peak obtained at higher energy value than the normal signal of Cu^{2+} (933.75 eV) is also termed as the shake-up peak. This is due to the fact that the outgoing electron interacts with the unpaired d-electron present in the $3d^9$ configuration of Cu^{2+} ions that 'shakes it' and falling some of its kinetic energy [30, 31]. Thus, a higher value energy peak emerges in spectra and often called as a shake-up peak. Also, the XPS signals of Cl 2p levels are also resolved into two peaks obtained at 197.51 and 198.84 eV (Fig. 4f) and are ascribed to the presence of AgCl [32]. The two peaks at 373.61 and 367.71 eV in Ag 3d XPS spectra, are assigned to Ag $3d_{3/2}$ and Ag $3d_{5/2}$ respectively. The obtained two signals are deconvoluted further into two signals at about 373.23/373.89 and 367.33/368.13 eV, respectively [33]. The peaks at 367.33 and 373.23 eV are due to Ag$^+$ of AgCl while the peaks at 368.13 and 373.89 eV are attributed to the metallic silver Ag^0 (Fig. 4g). According to the fitted XPS spectrum of Ag 3d, ratio of Ag$^+$ to Ag^0 in the BCA-2 composite was calculated to be 1:1.3. The excess amount of Ag^0 may be resulted by the reduction of AgCl on the
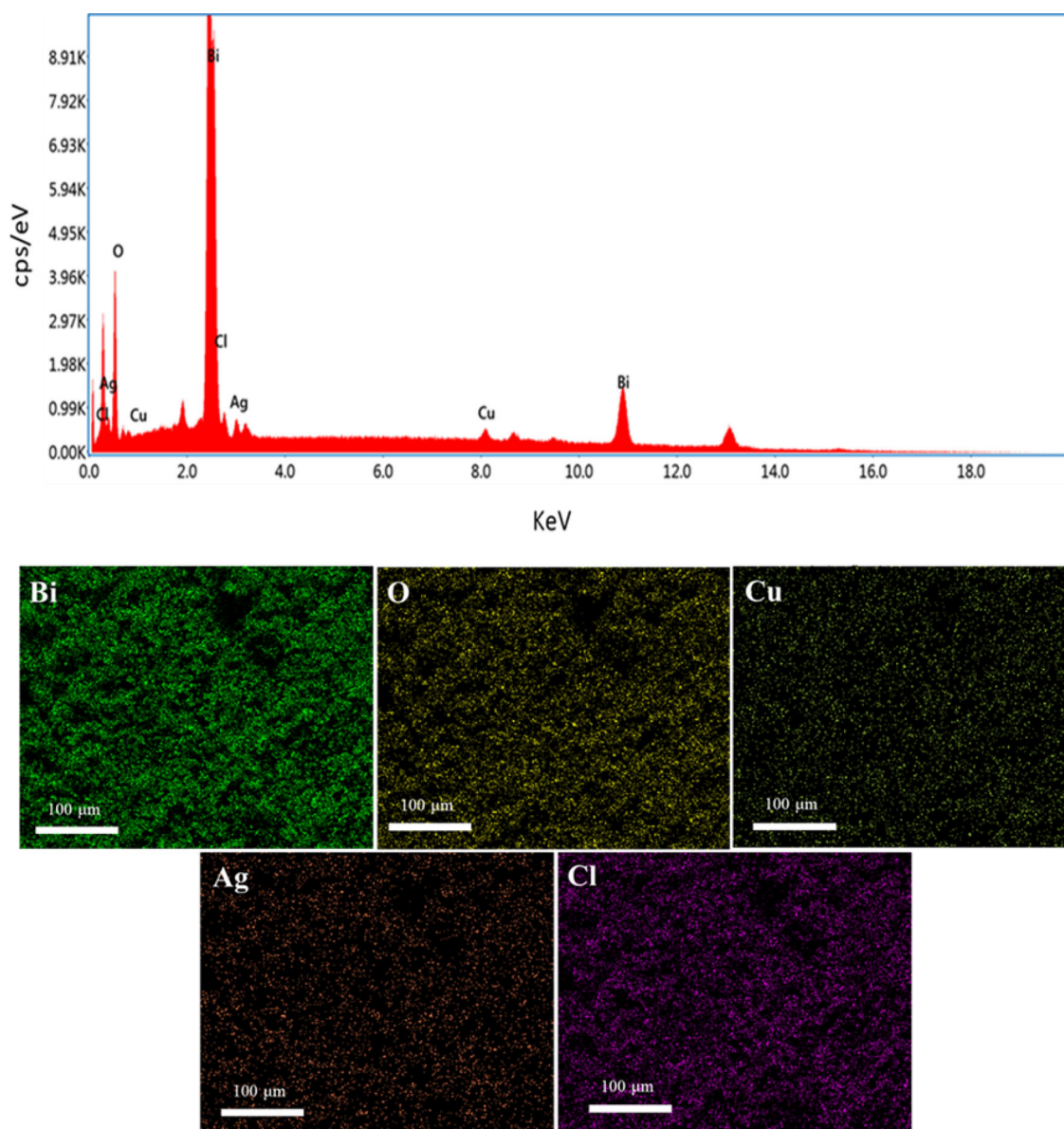
**Fig. 3** Elemental composition and mapping in EDX spectra of the sample BCA-2

surface. Therefore, the sample containing more content of Ag^0 on the surface i.e. BCA-3 showed lower photocatalytic efficiency [33]. Thus, the enhancement of catalytic efficiency of the composite BCA-2 is attributed to the role of Ag–AgCl nanocrystals.

3.4 FTIR analysis

To explore the bonding states of the elements, FTIR spectra were recorded (500–4000 cm^{-1}) and provided structural evidence for the synthesized nanocomposites (Fig. 5). The peak at 845 cm^{-1} signified vibrations of Bi-O-Bi and the two peaks obtained in the range 500–700 cm^{-1} correspond to Bi-O bonds of BiO_6 octahedron [34, 35]. However, no Cu–O bonds were detected in the spectra due to the relatively low content of the doped ions. The peak obtained at about 840 cm^{-1} can be approved to the Ag–Cl stretching vibration [36]. The peak obtained around 400 cm^{-1} corresponds to Ag metal [37].

3.5 Optical analysis (UVDRS)

Among the different optical methods, measuring diffuse reflectance of the powdered sample is one of the most important techniques to scrutinize the optical properties of the semiconductor materials. Indeed, UVDRS is a helpful spectroscopic device to calculate the optical band gaps of powdered samples. UV- DRS behaviour of all the prepared compounds are displayed in Fig. 6. The calculated
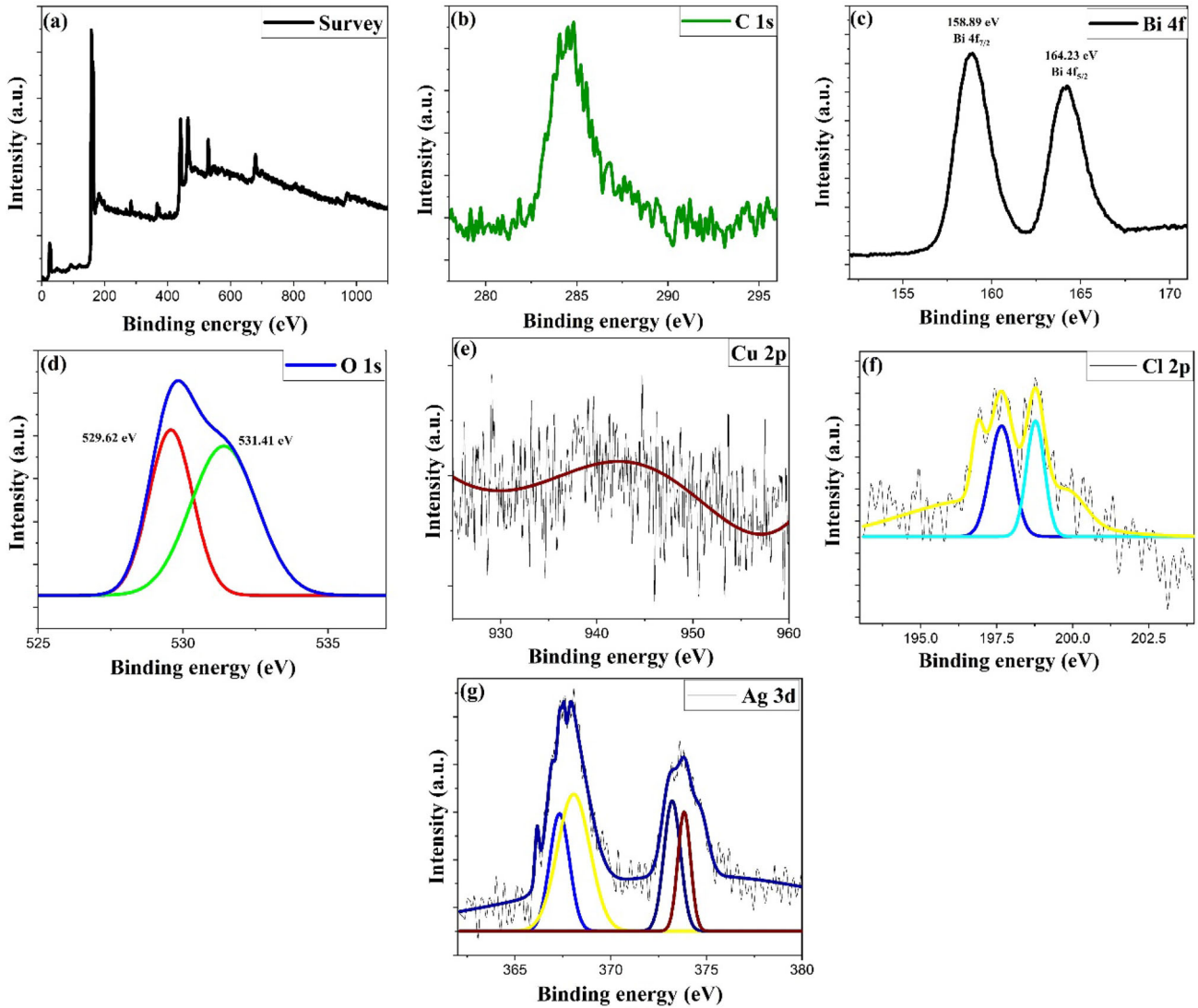
Fig. 4 High-resolution XPS characterization the of BCA-2 composite

Fig. 5 FTIR spectra of all the synthesized samples
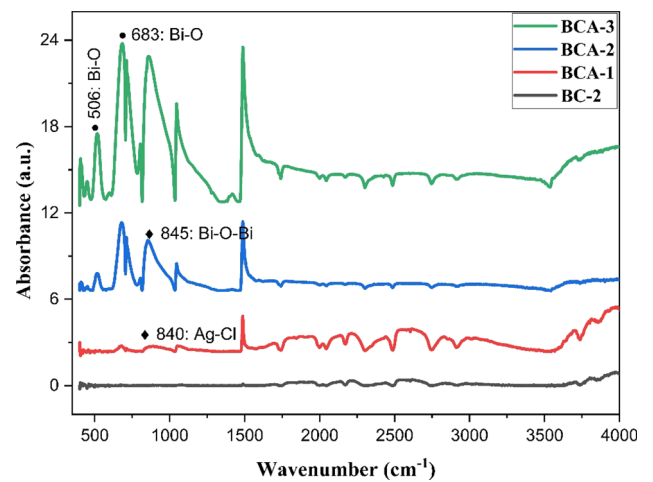
band gaps are found to be 3.42, 3.33, 3.59, and 3.57 eV for BC-2, BCA-1, BCA-2, and BCA-3 respectively. Thus, according to the calculated band gap values (3.42, 3.33, 3.59, and 3.57 eV); we need to use a UV light source in order to look into the photo-catalytic

Fig. 6 UV–Visible DRS spectra of all the synthesized samples
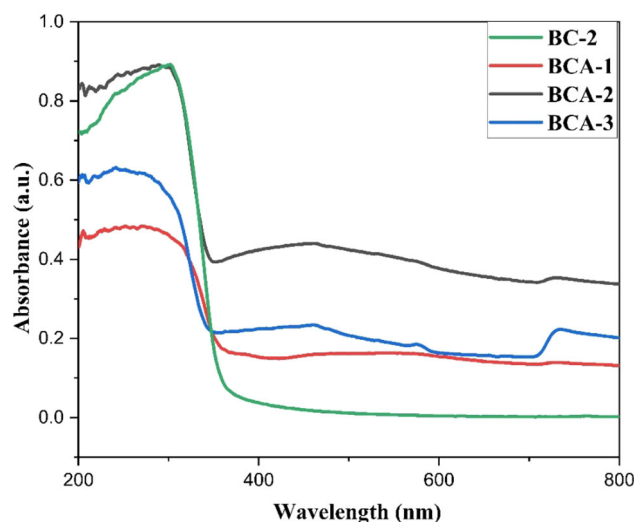
Fig. 7 Photoluminescence spectra of **a** binary BC-2 compared with all ternary compounds and **b** ternary BCA-1, BCA-2, and BCA-3 nanocomposites
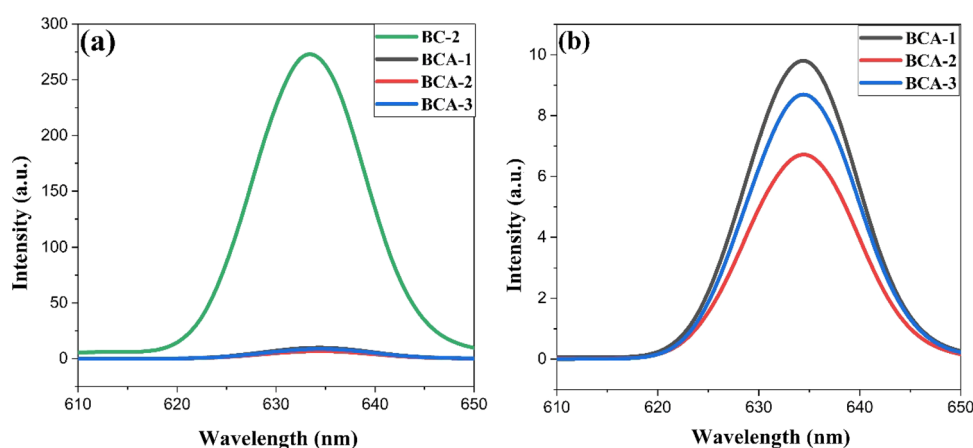
performance of the synthesized materials. Among all the samples, the BCA-2 composite showed the highest absorption intensity in the UV light region and is responsible for the highest catalytic efficiency in the degradation process [38].

3.6 PL emission spectra

It is well established that photocatalysts produce charge carriers (electrons and holes) when irradiated by UV light, and when recombination of these species takes place; energy is released as fluorescence emission. Thus, lower intensity of fluorescence emission signal implies the lower reunion rate of the electron–hole pairs [39]. Figure 7 displays the PL emission of all the prepared samples ($\lambda_{ex.}$315nm). It is clear that all the ternary samples exhibited decreased intensity of emission peaks than binary one wherein the sample BCA-2 showed maximum downturn in PL intensity, therefore explaining the highest photo-degradation efficiency of this nanocomposite [40].
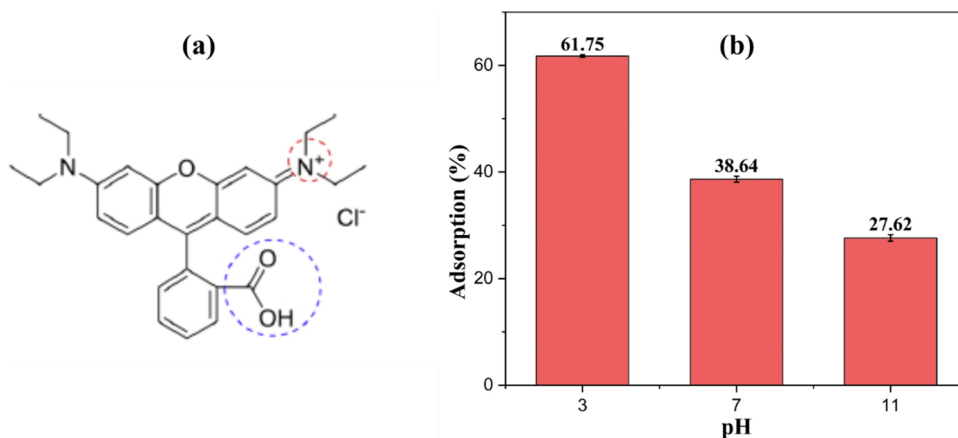
4 Adsorption study

Adsorptive removal of RhB dye from aqueous medium was studied using the prepared BCA- nanocomposites as the adsorbents. Highest adsorption was shown by the BCA-2 sample and was used in further studies. The adsorbed amounts of the dye were calculated with the help of the obtained concentration values [41]. The effects of medium pH, and temperature were studied in detail.

4.1 Effect of pH

pH of the aqueous medium directly influences the adsorption; especially in the case of RhB owing to its zwitterion structure. The adsorbent surface interacts with dye molecules via three fundamental interactions (1) electrostatic forces, (2) hydrophobic

Fig. 8 a Chemical structure of Rhodamine B and **b** RhB adsorption (%) using BCA-2 composite at different pH (3, 7, and 11)

Fig. 9 a Effect of temperature on adsorption efficiency and **b** Vant's Hoff plot (Initial concentration: 10 mg/L, dosage: 50 mg in neutral conditions)
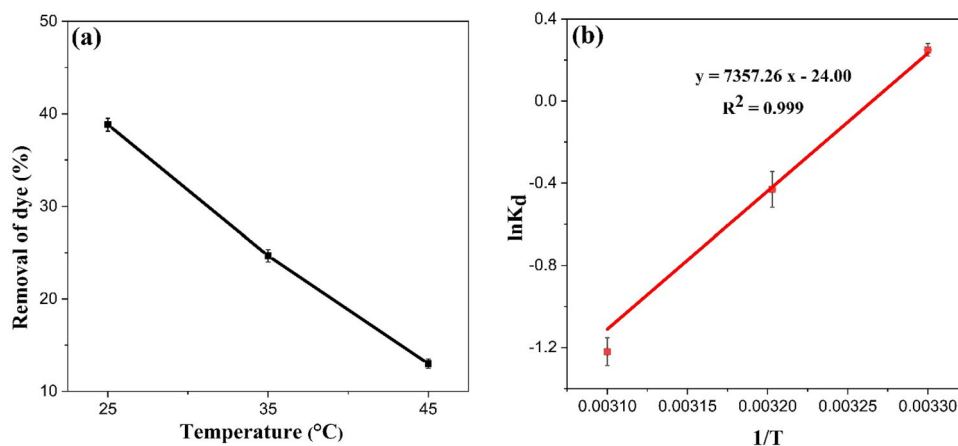
interactions, and (3) hydrogen bonding interactions. The interaction forces by RhB entirely change on changing the medium pH due to the formation of varying ionic species at different pH values [42]. Thus, pH effect on RhB adsorption by BCA-2 nanocomposite was studied in acidic, neutral, and basic mediums at $pH = 3$, 7, and 11 respectively keeping all other parameters constant. The results indicated maximum adsorption at $pH = 3$ and minimum at $pH = 11$ (Fig. 8).

In acidic pH, RhB exists in cationic form due to the protonation of COO^- functional group into COOH and the resulting hydrogen bonding interactions of this group with the adsorbent are responsible for higher adsorption of dye [43]. At pH greater than 5.5, zwitterionic form of RhB is found in the form of aggregated dimers. Therefore, these larger molecules are not able to enter into the pores of the adsorbent easily and thus decreased adsorption at $pH = 7$ [44]. On further increasing the $pH (= 11)$, adsorption is again decreased due to the appearance of negative charge on the adsorbent that lead to electrostatic repulsions between RhB and the adsorbent [45].

4.2 Adsorption thermodynamics

To examine the effect of temperature and calculate various thermodynamic parameters, adsorption experiments were performed between 25 to 45 °C. The system was examined for 60 min using 10 mg/L dye solution with 50 mg adsorbent dosage and pH maintained at neutral conditions. A noticeable decrease in removal efficiency was observed at higher temperatures (Fig. 9a), which suggests exothermic nature of the adsorption. This kind of behaviour may be ascribed to the weak forces of interaction between RhB molecules and the active sites of the adsorbent [46].

The thermodynamic parameters ($\Delta G°$, $\Delta H°$, and $\Delta S°$) were computed to study the interaction between adsorbate and adsorbent, feasibility and spontaneity of the process with the help of Van't Hoff equation. The plot was drawn between $ln K_d$ and $1/T$ (Fig. 9b) where slope and intercept represent the enthalpy change and entropy change respectively. The $\Delta G°$ values were then calculated by using the standard equations [46, 47].

Negative 1H° (− 61.13 kJ/mol) indicates the exothermic adsorption and more negative value of $\Delta S°$ (− 199.53 J/K/mol) suggested decrease in the randomness at the interface and thus stability of RhB on the adsorbent surface [46, 48]. The calculated $\Delta G°$ were − 0.619 (298 K), 1.101 (308 K), and 3.22 (318 K) respectively. The more negative value at 298 K (− 0.619 kJ/mol) indicated the spontaneity of the process at lower temperature as compared to the higher temperatures.

Fig. 10 Isotherm plots of adsorption of RhB
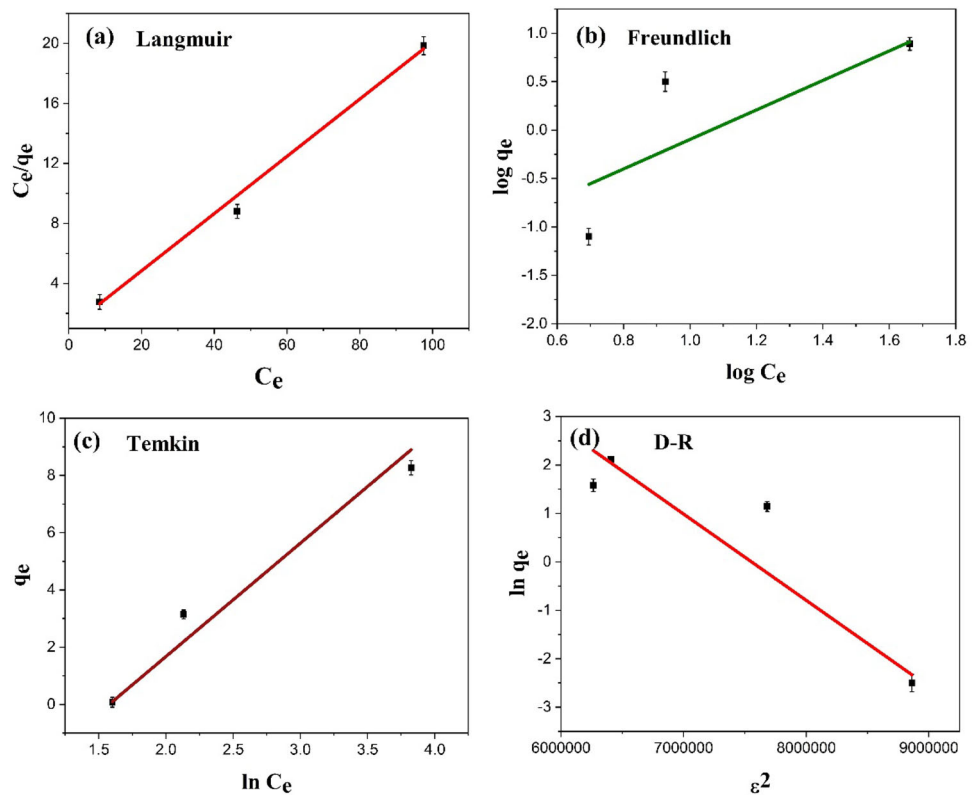
**Table 2** The adsorption isotherm parameters of different kinetic models for RhB

Isotherm model	Parameters	Value
Langmuir	b in (L/mg) q_m in (mg/g) R^2	0.185 ± 0.90 5.263 ± 0.25 0.997
Freundlich	K_F (mg/g (L/mg)$^{1/n}$) n R^2	0.024 ± 1.20 0.656 ± 0.82 0.774
Temkin	A in (L/g) B in (J/mol) R^2	0.208 ± 1.20 3.959 ± 0.72 0.967
Dubinin-Radushkevich (D-R)	β in (mol/K^2/J^2) E in (kJ/mol) R^2	1.580 ± 4.90 0.560 ± 0.45 0.836

4.3 Adsorption isotherms

To examine the nature of adsorption process isotherm models named Freundlich, Langmuir, Dubinin-Radushkevich (D-R) and Temkin were employed (Fig. 10) and the corresponding linear fitting outcomes are presented in Table 2.

As it is clear from the table, the highest value of R^2 (0.997) obtained in Langmuir model make it the best isotherm that is followed and is supported from literature [49, 50]. Therefore, uniform and single layer adsorption with same energy on all the sites is indicated [51]. To examine the heterogeneity of the adsorbent surface Freundlich model was used [52] and the results (Table 2) did not presented good linear correlation when compared to the Langmuir isotherm. The Temkin model states the free energy of adsorption shows a linear decrease with surface coverage [53] and the corresponding R^2 was obtained to be 0.967. In D-R adsorption model, if E value is lower than 8 kJ/mol, the adsorption is said to be of physical nature and if it is greater than or equal to 8 but < 16 kJ/mol, the adsorption is considered chemical adsorption [54]. The obtained E value in the present case (0.560 kJ/mol) indicated physiosorption of dye molecules on the adsorbent surface.

Fig. 11 Kinetic plots of adsorption of RhB
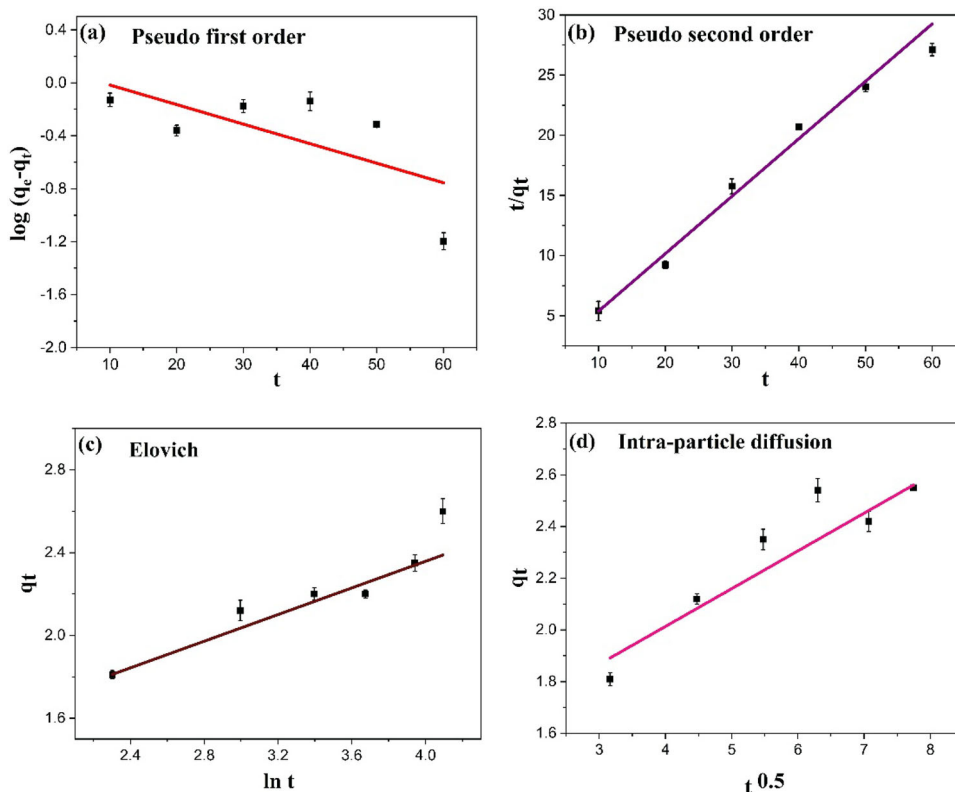
**Table 3** The Kinetic parameters of different models for RhB adsorption

Model	Parameters	Value
PFO	k_1 in (min^{-1})	0.035 ± 0.02
	q_e in (mg/g)	1.348 ± 0.30
	R^2	0.457
Elovich model	A in (mg/g/min)	1.071 ± 0.10
	B in (g/mg)	0.321 ± 0.01
	R^2	0.932
PSO	k_2 in (g/mg/ min)	3.509 ± 1.02
	q_e in (mg/g)	2.237 ± 0.05
	R^2	0.984
Intra-particle diffusion model	K_{id} in $(\text{mg/gmin}^{-1/2})$	0.146 ± 0.01
	I	1.429 ± 0.10
	R^2	0.880

4.4 Kinetic Studies

Kinetic studies of RhB adsorption were carried out using different models like pseudo-first order (PFO), pseudo-second order (PSO), intra-particle diffusion model, and Elovich model (Fig. 11). Table 3 lists the kinetics parameters obtained from these models.

From Table 3, the highest value of R^2 was found 0.984 in PSO kinetic model compared with the other models. Therefore, the pseudo-second order (PSO) kinetic model is the best model for adsorption. The value of I in Intra-particle diffusion model gives the information about the boundary layer effect [55] where calculated value of I being non-zero indicates increased effect of boundary layers. The deviation from the origin in the plot suggests some other mechanisms like pore diffusion, surface adsorption, and film diffusion [56] as the rate control steps other than the intra- particle diffusion.

Fig. 12 a Photocatalytic activities and **b** pseudo-first order kinetic of the degradation of binary (BC-2) and all the prepared ternary nanocomposites
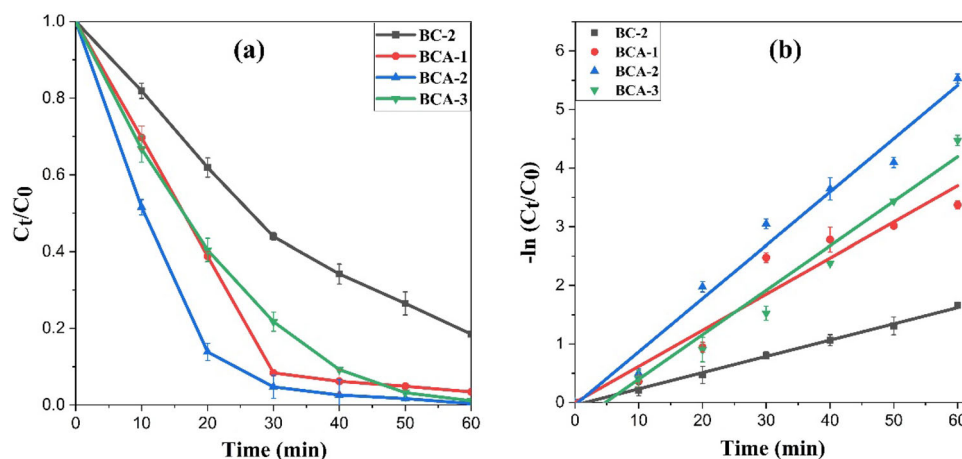
Table 4 Comparison of dye photo-degradation of Ag–AgCl-Bi$_2$O$_3$ materials with reported literature

Catalyst	Synthesis method	Morphology	Degradation efficiency (%)	Reference
Ag@AgCl/Cu^{2+}-Bi$_2$O$_3$	Hydrothermal-precipitation-reduction	Nano-flakes	99.60 in 60 min	Present study
Ag/AgCl/ BiOCl	Solvothermal	Flower-like	97.00% in 50 min	[28]
Ag/Ti-Doped-Bi$_2$O$_3$	Framework replacement	Spherical and ellipsoidal	91.50% in 80 min	[60]
AgCl/Ag/g-C$_3$N$_4$	Deposition–precipitation	Lamellar	99.00% in 60 min	[61]
Ag/AgCl/ Bi$_{20}$TiO$_{32}$	Deposition–precipitation	Nanosheets	98.90% in 25 min	[19]
Ag/AgCl/GO	Precipitation	Cubes-film	98.50% in 12 min	[62]
α/β-Bi$_2$O$_3$–Ag–AgCl	Precipitation- deposition	Nanowires- nanocrystals	98.00% in 20 min	[33]
Ag loaded Bi$_2$O$_3$/montmorillonite	Wet impregnation	Nanoparticles distributed over MMT	100% in 50 min	[63]
Ag-β-Bi$_2$O$_3$	Simple chemical	Sphere-like	98% in 210 min	[64]

5 Photocatalytic evaluation

Photocatalytic activities of the synthesized BCA-1, BCA-2, BCA-3, and binary BC-2 compounds was examined by selecting the organic pollutant Rhodamine B. All experiments were conducted under the illumination of UV light source (125 W). The taken sample volumes at different intervals of time were monitored at the characteristic absorption wavelength of the dye i.e. 553 nm, where the left out amounts of dye at that time was calculated. The obtained results for all the synthesized samples toward the degradation of RhB are displayed in the Fig. 12a. It is clear that the concentration of dye in the aqueous solution continuously decreased with the exposure of light irradiation and all the ternary samples exhibited superior catalytic performance when compared to the binary BC-2 photocatalyst. The highest activity was obtained for the Ag@AgCl ternary composite i.e. BCA-2: approximately 99.60% of RhB was degraded in 60 min of light illumination. Initially, with increase in the silver content, the degradation rate of the dye increased up to an appropriate concentration (0.05 mmol) and then drops on further increment. This may be resulted by the increasing number of heterojunctions at the interfaces which facilitate the movement and separation of the light generated charge carriers [18]. However, at higher amounts of Ag^0, the degradation efficiency of the composite decreased as observed for the sample BCA-3. This might be attributed to aggregation of the particles that lead to poor contact of radiations with the photocatalyst. The better activity of the Ag@AgCl containing sample i.e. (BCA-2) than the BCA-1 which contains 100% AgCl is explained by the Surface Plasmon Resonance (SPR) effect of Ag^0 in the BCA-2 nanocomposite [57]. The polarization interactions with the semiconductor may change the charge distribution of Ag nanoparticles that would develop partial positive and negatively charged regions in metallic nanoparticles; close to and far from the metal–semiconductor interface, respectively [58]. Therefore, the boosted effect of increased absorption of the light radiations by SPR effect of the metal nanoparticles along with the polarization field appeared in by AgCl improves separation of electron–hole pairs and interfacial transfer [59] and thus, responsible for the highest degradation rate of BCA-2 nanocomposite among all the prepared samples. Table 4 compares the photo-degradation efficiencies of some previously reported similar types of catalytic systems with the present work.

Table 5 Regression constants, Rate constants, and degradation efficiencies (%) of the prepared compounds

Catalyst	Rate constant	Regression constant	Degradation efficiency (%)
BC-2	0.027 ± 0.007	0.996	81.48 ± 0.50
BCA-1	0.061 ± 0.006	0.934	96.56 ± 0.44
BCA-2	0.090 ± 0.005	0.997	99.60 ± 0.35
BCA-3	0.075 ± 0.006	0.973	98.85 ± 0.20

Fig. 13 a Effect of medium pH and **b** scavengers on the photo-degradation using BCA-2 composite
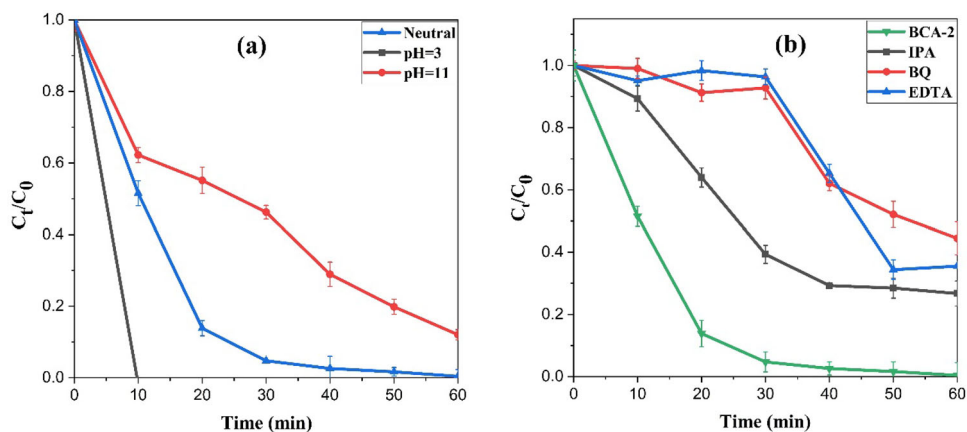
Kinetics of dye degradation process was examined on the basis of pseudo-first-order kinetic model, the corresponding apparent rate constants were determined by using the multiple linearly fitted curve as depicted in Fig. 12b. The rate constants, regression constants, and degradation efficiencies for all the synthesized compounds are listed in Table 5.

5.1 Effect of pH

pH of the reaction medium is a highly influential factor and effects the adsorption and hence degradation efficiency of the photocatalyst. This is because with change in pH of the reaction medium, surface charge on the compound i.e. photocatalyst gets changed. To examine pH effect, dye activities were performed in three different mediums (basic, acidic, and neutral) and obtained outcomes are presented in Fig. 13a. It is clear that the photocatalyst in the acidic medium exhibited the highest degradation toward the RhB; almost 100% just in 10 min while degradation rate was lowest in basic medium. To examine the surface charge on the sample under investigation, surface potentials were determined by using zeta potential analyzer. The photocatalyst exhibited positive potentials of 2.44 and 18.8 mV in acidic and neutral mediums respectively, whereas a negative value of − 30.3 mV was obtained in basic medium that are in fair agreement with the previous report [65, 66]. Therefore, normally it is expected that Rhodamine B being a cationic dye should show the electrostatic attraction with the negatively charged catalyst and can exhibit the higher degradation rate in basic medium, but that we observed is not the same. Because, in actual, it is decided by the pathway, the dye molecules breaks and further interacts with the surface of the catalyst, will really decide the degradation rate in a particular pH medium. In acidic medium, catalyst surface carries positive charge and therefore no positive interactions possible with the amino groups. On the other hand, hydrogen bonding interactions of carboxylic group in dye molecule with the catalyst surface allows electron injection and initiate the photosensitization [15, 67, 68]. Therefore, it is deduced that adsorption of dye via H-bonded –COOH groups on the catalytic surface played vital role in adsorption and hence degradation process in the acidic medium.

5.2 Role of scavengers

To detect the dominant active species in photocatalytic degradation of RhB, the degradation reactions were performed in the presence of some trapping agents including p-benzoquinone (BQ) is a scavenger for O_2^-, isopropanol (IPA) is a scavenger for $\cdot OH$, and ethylene diamine tetra-acetic acid (EDTA) can trap the hole respectively [69–71]. The obtained results are shown in the Fig. 13b and it is concluded that all the reactive species are appreciably contributing in the decolouration of RhB during the exposure of light. It is clear from the figure that maximum decrease in the activity was obtained when EDTA and BQ were used as compared to the IPA. Hence holes and superoxide anion radicals are found the premier species and they played prominent role in the degradation reaction.

Fig. 14 Schematic representation of energy levels, charge transfer and photocatalytic reactions
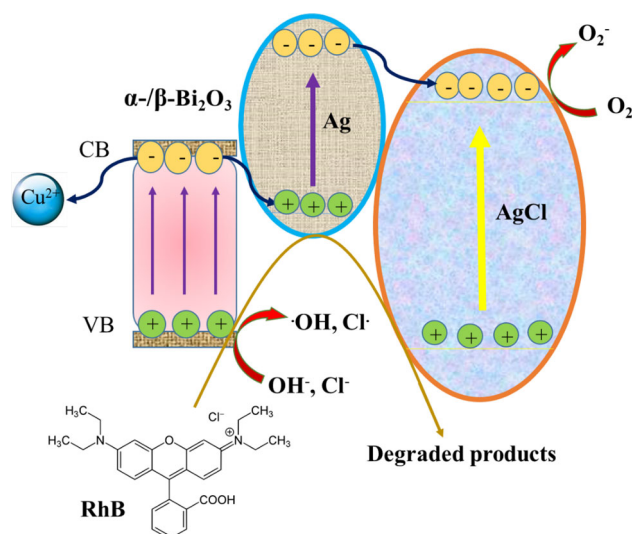
5.3 Adsorption and degradation mechanism

Based on above discussion, probable degradation mechanism of the dye was deduced (Fig. 14). The remarkable performance of $Ag@AgCl/Cu^{2+}-Bi_2O_3$ can be understood from different aspects. First of all, presence of Ag–AgCl nanocrystals on the surface are providing a number of interfaces between $Ag@AgCl$ and $Cu^{2+}-Bi_2O_3$ nanoparticles. Second, metallic silver nanoparticles formed on the semiconductors Bi_2O_3 and AgCl surfaces also contributed owing to the surface plasmonic resonance that generates transient holes and are capable to oxidize the dye molecules [72]. Apart from that, electron trapping by Cu^{2+} ions is also beneficial for the effectual separation of charged carriers. Further, positive synergistic effects of coupling Cu^{2+}- α–β -Bi_2O_3 with $Ag@AgCl$ delay the recombination of electron-holes and the probable routes of transfer of the charge-carriers. Due to the SPR effect and dipolar nature, metallic silver can efficiently absorb light radiations and lead to photo-generated electrons and holes [73, 74]. The Cu^{2+} ions present in the sample act as an electron scavenger (Fig. 14), decreasing recombination rate, and thus increasing lifetime of the charged species [75]. The plasmon-generated electrons in the silver are transferred to the conduction band of AgCl and converted the oxygen molecules to superoxide anion radicals. On the other side, holes are accumulated in the VB of Ag nanocrystals. The photo-generated electrons in α-β Bi_2O_3 move to the Ag particles to re-combine with the holes originated by plasmonic absorption whereas the holes in valence band remain on α-β Bi_2O_3 and utilized in oxidizing organic substances [76, 77]. Hence, the conduction band of AgCl acts as the reduction active site and valence band of α-β Bi_2O_3 is the oxidation active site in the degradation process.

6 Conclusion

In this experiment work, we successfully prepared a novel $Ag@AgCl$ decorated $Cu^{2+}–Bi_2O_3$ nanocomposite and examined for adsorption and photo-catalytic properties. The maximum dye adsorption (61.75%) was obtained at $pH = 3$. Further, the adsorption was described best by the Langmuir and pseudo second-order models for isotherm and kinetics, respectively. The thermodynamic results indicated the exothermic and spontaneous adsorption at lower temperatures. The results demonstrated that the catalyst exhibited superior activity in RhB removal and the dye was completely removed after 60 min light irradiation. The increased catalytic efficiency is largely accredited to the existence of a number of interfaces between $Ag@AgCl$ and $Cu^{2+}–Bi_2O_3$ nanoparticles leading to the effective separation of electron–hole pairs, and the surface plasmonic resonance effect of Ag nanoparticles. In the photocatalysis process, holes along with superoxide anion radicals are the prominent reactive species involved in degradation reaction as supported by the scavenger studies.

Data availability All data generated or analysed during this study are included in this published article.

Declarations

Conflict of interest On behalf of all the authors, the corresponding author states no conflict of interest.

References

1. S. Sharma, A. Mittal, N. Singh Chauhan, P. R. Makgwane, K. Kumari, S. Maken, and N. Kumar, Inorgan. Chem. Commun. **133**, 108874 (2021).
2. H.E. Emam, M. El-Shahat, R.M. Abdelhameed, J. Hazard. Mater. **414**, 125509 (2021)
3. R.M. Abdelhameed, A.A. Shaltout, M.H.H. Mahmoud, H.E. Emam, Sustain. Mater. Technol. **29**, e00326 (2021)
4. H.E. Emam, T.I. Shaheen, J. Polym. Environ. **27**, 2419 (2019)
5. S. Yadav, J. Jindal, A. Mittal, S. Sharma, K. Kumari, N. Kumar, J. Phys. Chem. Solids **157**, 110217 (2021)
6. S. Sharma, N. Kumar, B. Mari, N.S. Chauhan, A. Mittal, S. Maken, K. Kumari, Inorg. Chem. Commun. **125**, 108418 (2021)
7. S. Yadav, A. Mittal, S. Sharma, K. Kumari, N. Kumar, Inorg. Chem. Commun. **130**, 108738 (2021)
8. R. Hu, X. Xiao, S. Tu, X. Zuo, J. Nan, Appl. Catal. B **163**, 510 (2015)
9. X. Chen, J. Dai, G. Shi, L. Li, G. Wang, H. Yang, J. Alloy. Compd. **649**, 872 (2015)
10. L. Di, X. Sun, T. Xian, H. Li, Y. Gao, H. Yang, Adv. Powder Technol. **32**, 3672 (2021)
11. F. Yang, X. Yu, Z. Liu, K. Wang, Q. Ji, Y. Chen, T. Zhang, J. Niu, J. Zhao, B. Yao, Appl. Surf. Sci. **575**, 151757 (2022)
12. B. Jia, J. Zhang, J. Luan, F. Li, J. Han, J. Mater. Sci. Mater. Electron. **28**, 11084 (2017)
13. Y. Nie, Y. Xie, Y. Zheng, Y. Luo, J. Zhang, Z. Yi, F. Zheng, L. Liu, X. Chen, P. Cai, P. Wu, Coatings **11**, 1140 (2021)
14. Y. Li, S. Wu, L. Huang, H. Xu, R. Zhang, M. Qu, Q. Gao, H. Li, J. Phys. Chem. Solids **76**, 112 (2015)
15. A. Sharma, A. Mittal, S. Sharma, K. Kumari, S. Maken, N. Kumar, Appl Nanosci **12**, 151 (2022)
16. T. Morimoto, K. Suzuki, M. Torikoshi, T. Kawahara, and H. Tada, Chem. Commun. 4291 (2007).
17. P. Wang, B. Huang, X. Qin, X. Zhang, Y. Dai, M.-H. Whangbo, Inorg. Chem. **48**, 10697 (2009)
18. X.-J. Wen, C.-G. Niu, D.-W. Huang, L. Zhang, C. Liang, G.-M. Zeng, J. Catal. **355**, 73 (2017)
19. J. Hou, Z. Wang, C. Yang, W. Zhou, S. Jiao, H. Zhu, J. Phys. Chem. C **117**, 5132 (2013)
20. X. Meng, Z. Zhang, Int. J. Photoenergy **2016**, 1 (2016)
21. H. Oudghiri-Hassani, S. Rakass, F. T. Al Wadaani, K. J. Al-ghamdi, A. Omer, M. Messali, and M. Abboudi, Journal of Taibah University for Science **9**, 508 (2015).
22. J. Hou, C. Yang, Z. Wang, W. Zhou, S. Jiao, H. Zhu, Appl. Catal. B **142–143**, 504 (2013)
23. A. K. R. Police, S. V. P. Vattikuti, K. K. Mandari, M. Chennaiahgari, P. S. M.V., D. K. Valluri, and C. Byon, Ceramics International **44**, 11783 (2018).
24. P. Kumari, R.K. Das, B. Pal, Mater. Chem. Phys. **260**, 124173 (2021)
25. V. Kumari, S. Yadav, J. Jindal, S. Sharma, K. Kumari, N. Kumar, Adv. Powder Technol. **S092188312030**, 2020 (1886)
26. Y. Astuti, D. Amri, D.S. Widodo, H. Widiyandari, R. Balgis, T. Ogi, IJTech **11**, 26 (2020)
27. S. Balachandran, N. Prakash, M. Swaminathan, RSC Adv. **6**, 20247 (2016)
28. S. Zhao, Y. Zhang, Y. Zhou, K. Qiu, C. Zhang, J. Fang, X. Sheng, J. Photochem. Photobiol. A **350**, 94 (2018)
29. U.K. Gaur, A. Kumar, G.D. Varma, J. Mater. Chem. C **3**, 4297 (2015)
30. N. Kamarulzaman, M.F. Kasim, N.F. Chayed, Result. Phys. **6**, 217 (2016)
31. P.A.W. van der Heide, J. Electron. Spectrosc. Relat. Phenom. **164**, 8 (2008)
32. R. Dong, B. Tian, C. Zeng, T. Li, T. Wang, J. Zhang, J. Phys. Chem. C **117**, 213 (2013)
33. H. Cheng, J. Hou, H. Zhu, X.-M. Guo, RSC Adv. **4**, 41622 (2014)
34. J. Yang, T. Xie, C. Liu, L. Xu, Materials **11**, 1359 (2018)
35. P. Raizada, P. Thakur, A. Sudhaik, P. Singh, V.K. Thakur, A. Hosseini-Bandegharaei, Arab. J. Chem. **13**, 4538 (2020)
36. P. Panchal, P. Meena, S.P. Nehra, Environ. Sci. Pollut. Res. **28**, 3972 (2021)
37. O. Pawar, N. Deshpande, S. Dagade, S. Waghmode, and P. Nigam Joshi. J. Exp. Nanosci. **11**, 28 (2016)
38. Q. Wang, J. Hui, L. Yang, H. Huang, Y. Cai, S. Yin, Y. Ding, Appl. Surf. Sci. **289**, 224 (2014)
39. A. Phuruangrat, S. Jonjana, S. Thongtem, T. Thongtem, J. Aust. Ceram. Soc. **55**, 57 (2019)
40. M. Du, S. Zhang, Z. Xing, Z. Li, J. Yin, J. Zou, Q. Zhu, W. Zhou, Langmuir **35**, 7887 (2019)
41. R.M. Abdelhameed, M. Taha, H. Abdel-Gawad, H.E. Emam, J. Mol. Struct. **1250**, 131914 (2022)
42. L.P. Hoang, H.T. Van, T.T.H. Nguyen, V.Q. Nguyen, P. Quang Thang, J. Chem. **2020**, 1 (2020)
43. A. A. Inyinbor, F. A. Adekola, and G. A. Olatunji, S. Afr. J. Chem **68**, (2015).
44. L. Ding, B. Zou, W. Gao, Q. Liu, Z. Wang, Y. Guo, X. Wang, Y. Liu, Colloids Surf., A **446**, 1 (2014)
45. R. Rubab, S. Ali, A.U. Rehman, S.A. Khan, A.M. Khan, Colloids Surf. A **615**, 126253 (2021)
46. J. Aravind Kumar, T. Krithiga, K. Vijai Anand, S. Sathish, S. Karthick Raja Namasivayam, A. A. Renita, A. Hosseini-Bandegharaei, T. R. Praveenkumar, M. Rajasimman, N. S. Bhat, and S. Dutta, J. Mole. Liq. **334**, 116080 (2021).
47. Y. Wang, J. Li, Y. Yuan, Y. Si, J. Xu, M. Li, X. Peng, Colloids Surf. A **626**, 127060 (2021)
48. D.L. Postai, C.A. Demarchi, F. Zanatta, D.C.C. Melo, C.A. Rodrigues, Alex. Eng. J. **55**, 1713 (2016)
49. R.M. Abdelhameed, H.E. Emam, Sustain. Mater. Technol. **31**, e00366 (2022)
50. H.E. Emam, M. El-Shahat, M. Taha, R.M. Abdelhameed, Surfaces and Interfaces **30**, 101940 (2022)
51. A. Sharma, Z.-M. Siddiqi, D. Pathania, J. Mol. Liq. **240**, 361 (2017)
52. S. Sharifnia, M.A. Khadivi, T. Shojaeimehr, Y. Shavisi, J. Saudi Chem. Soc. **20**, S342 (2016)
53. H. Naeem, M. Ajmal, R.B. Qureshi, S.T. Muntha, M. Farooq, M. Siddiq, J. Environ. Manag. **230**, 199 (2019)
54. R. Ahmad, K. Ansari, Process Biochem. **108**, 90 (2021)
55. R. Ahmad, S. Haseeb, J. Dispersion Sci. Technol. **33**, 1188 (2012)
56. F. Zhang, B. Ma, X. Jiang, Y. Ji, Powder Technol. **302**, 207 (2016)
57. H. Derikvandi, M. Vosough, A. Nezamzadeh-Ejhieh, Int. J. Hydrogen Energy **46**, 2049 (2021)
58. S. Zhang, J. Li, X. Wang, Y. Huang, M. Zeng, J. Xu, A.C.S. Appl, Mater. Interfaces **6**, 22116 (2014)
59. H. Dongliang, H. Jiahai, Q. Long, P. Jiangrui, S. Zhenji, Rare Metal Mater. Eng. **44**, 1888 (2015)
60. L. Zhang, J. Niu, D. Li, D. Gao, J. Shi, Adv. Conden. Matter Phys. **2014**, 1 (2014)
61. Y. Bao, K. Chen, Nano-Micro Lett. **8**, 182 (2016)
62. L. Liu, J. Deng, T. Niu, G. Zheng, P. Zhang, Y. Jin, Z. Jiao, X. Sun, J. Colloid Interface Sci. **493**, 281 (2017)
63. P.P. Tun, J. Wang, T.T. Khaing, X. Wu, G. Zhang, J. Alloy. Compd. **818**, 152836 (2020)
64. G. Zhu, W. Que, J. Zhang, J. Alloy. Compd. **509**, 9479 (2011)
65. M. Kosmulski, Adv. Coll. Interface. Sci. **152**, 14 (2009)
66. T.A. Gadhi, A. Hernández-Gordillo, M. Bizarro, P. Jagdale, A. Tagliaferro, S.E. Rodil, Ceram. Int. **42**, 13065 (2016)
67. O. Merka, V. Yarovyi, D.W. Bahnemann, M. Wark, J. Phys. Chem. C **115**, 8014 (2011)

68. A. Mittal, S. Sharma, V. Kumari, S. Yadav, N.S. Chauhan, N. Kumar, J. Mater. Sci. Mater. Electron. **30**, 17933 (2019)
69. H.E. Emam, H.B. Ahmed, E. Gomaa, M.H. Helal, R.M. Abdelhameed, Cellulose **27**, 7139 (2020)
70. S. Yadav, N. Kumar, V. Kumari, A. Mittal, S. Sharma, Mater. Today Proceed. **19**, 642 (2019)
71. S. Yadav, A. Mittal, S. Sharma, K. Kumari, N.S. Chauhan, N. Kumar, Semicond. Sci. Technol. **35**, 055008 (2020)
72. X. Gao, Y. Shang, L. Liu, K. Gao, J. Alloy. Compd. **803**, 565 (2019)
73. X. Jiang, Y. Zhang, J. Jiang, Y. Rong, Y. Wang, Y. Wu, C. Pan, J. Phys. Chem. C **116**, 22619 (2012)
74. Y. Yang, W. Guo, Y. Guo, Y. Zhao, X. Yuan, Y. Guo, J. Hazard. Mater. **271**, 150 (2014)
75. W. Qin, J. Qi, X. Wu, Vacuum **107**, 204 (2014)
76. H. Wang, X. Yang, J. Zi, M. Zhou, Z. Ye, J. Li, Q. Guan, P. Lv, P. Huo, Y. Yan, J. Ind. Eng. Chem. **35**, 83 (2016)
77. W. Wu, J. Wang, T. Zhang, S. Jiang, X. Ma, G. Zhang, X. Zhang, X. Chen, B. Li, J. Mater. Chem. C **7**, 5451 (2019)